Weierstraß-Institut
für Angewandte Analysis und Stochastik
Leibniz-Institut im Forschungsverbund Berlin e. V.

Preprint ISSN 0946 – 8633

A numerical method for the simulation of an aggregation-driven population balance system

Wolfgang Hackbusch[1], Volker John [2,3], Aram Khachatryan[1], Carina Suciu[2]

submitted: June 21, 2011

[1] Max-Planck-Institute for Mathematics in the Sciences
Inselstr. 22-26
04103 Leipzig
Germany
email: wh@mis.mpg.de
email: khachatr@mis.mpg.de

[2] Weierstrass Institute
Mohrenstr. 39
10117 Berlin
Germany
email: Volker.John@wias-berlin.de
email: Carina.Suciu@wias-berlin.de

[3] Free University of Berlin
Department of Mathematics and Computer Science
Arnimallee 6
14195 Berlin
Germany

No. 1621

Berlin 2011

2010 *Mathematics Subject Classification.* 45K05, 44A35.

Key words and phrases. Population balance systems, aggregation, integro partial differential equation, stabilised methods, convolution, calibration of parameters.

Edited by
Weierstraß-Institut für Angewandte Analysis und Stochastik (WIAS)
Leibniz-Institut im Forschungsverbund Berlin e. V.
Mohrenstraße 39
10117 Berlin
Germany

Fax: +49 30 2044975
E-Mail: preprint@wias-berlin.de
World Wide Web: http://www.wias-berlin.de/

Abstract

A population balance system which models the synthesis of urea is studied in this paper. The equations for the flow field, the mass and the energy balances are given in a three-dimensional domain and the equation for the particle size distribution (PSD) in a four-dimensional domain. This problem is convection-dominated and aggregation-driven. Both features require the application of appropriate numerical methods. This paper presents a numerical approach for simulating the population balance system which is based on finite element schemes, a finite difference method and a modern method to evaluate convolution integrals that appear in the aggregation term. Two experiments are considered and the numerical results are compared with experimental data. Unknown parameters in the aggregation kernel have to be calibrated. For appropriately chosen parameters, good agreements are achieved of the experimental data and the numerical results computed with the proposed method. A detailed study of the computational results reveals the influence of different parts of the aggregation kernel.

1. INTRODUCTION

Many species in chemical or pharmaceutical processes are produced in particulate form. Rather than the behaviour of each individual particle, averaged properties of the particles are of interest in applications. Such averages can be described by particle size distributions (PSD) and the behaviour of PSDs can be modelled by population balance systems. Population balance systems describe, e.g., the nucleation, growth, aggregation, breakage and transport of particles. These are coupled systems consisting of, e.g., the Navier–Stokes equations, equations for mass and energy balances, and for the PSD. Whereas the flow field, concentrations of dissolved species and temperature depend on time and space, the PSD depends also on properties of the particles, the so-called internal coordinates. Altogether, a population balance system contains equations which are defined in domains with different dimension.

In applications, the domain for the flow field etc. is three-dimensional and the domain for the PSD at least four-dimensional. Of course, the accurate and efficient simulation of such population balance systems poses a great challenge. There are still only few approaches for the simulation of the equation for the PSD in the higher-dimensional domain [1, 2, 3, 4]. Currently more widely used are several proposals for model simplification, which replace the higher-dimensional equation for the PSD by a system of equations in three dimensions. The most popular approaches in this direction are the quadrature method of moments (QMOM) [5] and the direct quadrature method of moments (DQMOM) [6]. These methods approximate the first moments of the PSD. However, the reconstruction of a PSD from a finite number of its moments is a severely ill-posed problem [7, 8].

In our opinion, an accurate simulation of population balance systems requires the treatment of the coupled problem in three and four dimensions. It was already shown in [9, 10] that even with this approach, the use of different numerical methods might lead to considerable

*Correspondence to: volker.john@wias-berlin.de

Prepared using fldauth.cls DOI: 10.1002/fld

differences in computed outputs of interest. For this reason, it is important to simulate problems which allow the comparison of the computed results with experimental data.

This paper considers a laboratory experiment [11], a synthesis of urea particles, for which measurement data are available. A model for this process is provided which takes into account the transport, the growth and the aggregation of urea particles. From the point of view of chemical engineering, it is clear that the behaviour of the particles is driven by aggregation. Hence, the aggregation kernel is of utmost importance in the model. This kernel consists of two parts, one describing aggregation by Brownian motion and the other one describing shear-induced aggregation. A main goal of the numerical simulations was the calibration of two unknown model parameters in this kernel by comparing numerical results with experimental data.

An important aspect for reliable comparisons is the use of accurate numerical methods. Thus, the flow field will be simulated by a higher-order finite element method, the equations for the concentration of dissolved urea and for the temperature by one of the most accurate stabilised finite element methods [12], and the aggregation integrals are computed by a modern approach from [13, 14, 15]. Only the convective part of the equation for the PSD is discretised, for efficiency reasons, with a rather simple scheme, which, however, has proven to give very similar results to more complicated schemes in the presence of laminar flow fields [10]. With these methods, parameters for the aggregation kernel could be identified for two experimental setups which give results that agree well with the experimental data. Reasons for differences of the optimal parameters between both examples are discussed. Detailed studies of the PSD for different nodes of the grid at the outlet highlight the impact of the individual terms of the aggregation kernel.

The paper is organised as follows. Section 2 introduces the population balance system which models the urea synthesis. The numerical methods which are used in the simulations of the flow field, the temperature, the concentration and the convective part of the equation for the PSD, and the method that is used for computing the aggregation term are presented in Section 3.

Prepared using **fldauth.cls** DOI: 10.1002/fld

Then, Section 4 describes the incorporation of the experimental data into the simulations. The main part of the paper is Section 5, which contains the numerical studies, the comparisons with the experimental data and a discussion of the results. A summary and an outlook are given in Section 6.

2. THE POPULATION BALANCE MODEL OF THE UREA SYNTHESIS

The studied urea population is modelled by a system of equations describing the flow field (velocity, pressure), the energy balance (temperature), the mass balance (concentration) and the particle size distribution. The experimental setups, which were the basis of the numerical simulations, led to steady-state flow fields.

The flow field obeys the incompressible Navier–Stokes equations

$$\begin{aligned} -\mu\Delta\mathbf{u} + \rho\left((\mathbf{u}\cdot\nabla)\mathbf{u}\right) + \nabla p &= \rho\mathbf{g} \quad \text{in } \Omega, \\ \nabla\cdot\mathbf{u} &= 0 \quad \text{in } \Omega, \end{aligned} \tag{1}$$

where $\Omega = (0, 210) \times (0, 1) \times (0, 1)$ $\left[\mathrm{cm}^3\right]$ is the flow domain, $\mathbf{u}$ [m/s] is the fluid velocity, p [Pa] is the pressure, $\rho = 789$ $\left[\mathrm{kg/m}^3\right]$ is the density of ethanol, $\mu = 1.074 \cdot 10^{-3}$ [kg/(m s)] is the dynamic viscosity of ethanol (both at 298 K) and $\mathbf{g}$ [m/s^2] is the gravitational acceleration. In the experiments, the suspension is sufficiently dilute, the size of the particles is sufficiently small and the temperature gradient is also small enough such that the influence of all these aspects on the flow field can be neglected. The Navier–Stokes equations (1) has to be closed with boundary conditions. The boundary Γ of Ω is the union of the inlet boundary $\Gamma_{\text{in}} = \{0 \text{ cm}\} \times (1/3 \text{ cm}, 2/3 \text{ cm}) \times (1/3 \text{ cm}, 2/3 \text{ cm})$, the outlet boundary $\Gamma_{\text{out}} = \{210 \text{ cm}\} \times (0 \text{ cm}, 1 \text{ cm}) \times (0 \text{ cm}, 1 \text{ cm})$ and the walls $\Gamma_{\text{wall}} = \Gamma \setminus (\Gamma_{\text{in}} \cup \Gamma_{\text{out}})$. The unit outer normal vector on the boundary is denoted by $\mathbf{n}_\Gamma$. The exact conditions at the inlet Γ_{in} are not known, only the flow rates at the inlet. A simple approach would be the application of plug flows (constant velocities) at the inlet that matches the given flow rates. But this approach leads to jumps in the boundary condition. This is certainly not correct since no-slip boundary conditions hold at the boundaries of the supply to the flow domain. For this

DOI: 10.1002/fld

reason, an inlet boundary condition of the form

$$\mathbf{u}(\mathbf{x}) = U_{\text{in}}(\Psi(\xi,\eta),0,0)^T, \quad \mathbf{x} \in \Gamma_{\text{in}}, \tag{2}$$

was used, where the profile $\Psi(\xi,\eta)$ of this condition is the solution of the two-dimensional Poisson equation

$$-\Delta\Psi = 1 \text{ in } \Gamma_{\text{in}}, \quad \Psi = 0 \text{ on } \partial\Gamma_{\text{in}}.$$

The parameter U_{in} was chosen to match the experimental inflow rates, see Section 4. The boundary condition at the outlet Γ_{out} is the standard do-nothing condition

$$(\mu\nabla(\mathbf{u}) - p\mathbb{I}) \cdot \mathbf{n}_\Gamma = \mathbf{0}, \quad \mathbf{x} \in \Gamma_{\text{out}}, \tag{3}$$

that is often used in numerical simulations [16]. A boundary condition at the outlet is not known from the experiments. In particular, it is unclear how good this unknown boundary condition corresponds to (3). For this reason, the length of the computational domain was chosen larger than the length of the experimental domain (210 cm instead of 200 cm) such that a possible slight incorrectness of the outflow boundary condition (3) does not possess an influence on the computational results in the region that corresponds to the outlet of the experimental domain. At all other boundaries (the walls), the no-slip condition

$$\mathbf{u}(\mathbf{x}) = \mathbf{0}, \quad \mathbf{x} \in \Gamma_{\text{wall}}, \tag{4}$$

was applied.

The mass balance of the system is given by

$$\frac{\partial c}{\partial t} - D\Delta c + \mathbf{u}\cdot\nabla c + \frac{3\rho^d k_V G(c,T)}{m_{\text{mol}}} \int_{L_{\min}}^{L_{\max}} L^2 f \, dL = -\frac{\rho^d k_V L_{\min}^3 B_{\text{nuc}}}{m_{\text{mol}}} \text{ in } (0,t_e)\times\Omega. \tag{5}$$

In (5), c [mol/m^3] is the concentration of urea in the suspension, $D = 1.35 \cdot 10^{-9}$ $\left[\text{m}^2/\text{s}\right]$ is the diffusion coefficient of urea in ethanol, $\rho^d = 1323$ $\left[\text{kg/m}^3\right]$ is the density of urea (dispersed phase), $k_V = \pi/6$ $[\cdot]$ is the scaling factor from diameters to volume (where it is assumed that all particles are balls), $G(c,T)$ [m/s] is the growth rate given below in (8), T [K] is the temperature, $m_{\text{mol}} = 60.06 \cdot 10^{-3}$ [kg/mol] is the molar mass of urea, $B_{\text{nuc}} = 10^8$ [1/(m^3 s)] is

DOI: 10.1002/fld

a constant nucleation rate and t_e [s] is a final time. The diameter of the particles is denoted by L [m], where $L_{\min}$ is the smallest diameter (nuclei size) and $L_{\max}$ is an upper bound for the largest diameter. The particle size distribution is f $\left[1/\mathrm{m}^4\right]$. The last term on the left hand side of (5) models the decrease of dissolved urea due to the growth of particles and the term on the right hand side describes the consumption of dissolved urea due to the nucleation of particles. Equation (5) has to be equipped with initial and boundary conditions. The boundary condition is given by

$$\left\{\begin{array}{rcll} c(t,\mathbf{x}) & = & c_{\mathrm{sat}}(T_{\mathrm{in}}), & \mathbf{x}\in\Gamma_{\mathrm{in}}, \\ D\dfrac{\partial c}{\partial \mathbf{n}_\Gamma} & = & 0, & \mathbf{x}\in\Gamma_{\mathrm{out}}\cup\Gamma_{\mathrm{wall}}, \end{array}\right. \tag{6}$$

with the saturation concentration

$$c_{\mathrm{sat}}(T) = \frac{35.364 + 1.305(T - 273.15)}{m_{\mathrm{mol}}} \left[\frac{\mathrm{mol}}{\mathrm{m}^3}\right]. \tag{7}$$

With this boundary condition, (5) without the coupling terms to the PSD is solved until a steady state is reached. This steady state is used as initial condition $c(0,\mathbf{x})$. The growth rate is given by

$$G(c,T) = \begin{cases} k_g\left(\dfrac{c - c_{\mathrm{sat}}(T)}{c_{\mathrm{sat}}(T)}\right)^g, & \text{if } c > c_{\mathrm{sat}}(T), \\ 0, & \text{else}, \end{cases} \tag{8}$$

with the growth rate constant $k_g = 10^{-7}$ [m/s] and the growth rate power $g = 0.5$ [$\cdot$].

Next, the energy balance is modelled by

$$\begin{array}{rl} & -\lambda\Delta T + \rho c_p\left(\dfrac{\partial T}{\partial t} + \mathbf{u}\cdot\nabla T\right) + 3\Delta h_{\mathrm{cryst}}\rho^d k_V G(c,T)\displaystyle\int_{L_{\min}}^{L_{\max}} L^2 f\, dL \\ = & -\Delta h_{\mathrm{cryst}}\rho^d k_V L_{\min}^3 B_{\mathrm{nuc}} \text{ in } (0,t_e)\times\Omega, \end{array} \tag{9}$$

where $c_p = 2441.3$ [J/(kg K)] is the specific heat capacity of ethanol, $\lambda = 0.167$ [J/(K m s)] is its thermal conductivity and $\Delta h_{\mathrm{cryst}} = 2.1645 \cdot 10^5$[J/kg] is the heat of solution (enthalpy change of solution). The boundary conditions are known from the experiments

$$\left\{\begin{array}{rcll} T(t,\mathbf{x}) & = & T_{\mathrm{in}}, & \mathbf{x}\in\Gamma_{\mathrm{in}}, \\ \lambda\dfrac{\partial T}{\partial \mathbf{n}_\Gamma} & = & 0, & \mathbf{x}\in\Gamma_{\mathrm{out}}, \\ T(t,\mathbf{x}) & = & T_{\mathrm{wall}}, & \mathbf{x}\in\Gamma_{\mathrm{wall}}, \end{array}\right. \tag{10}$$

Prepared using **fldauth.cls** DOI: 10.1002/fld

with $T_{\text{in}} = 301.15$ [K] and $T_{\text{wall}} = 291.15$ [K]. Hence, the suspension is cooled at the wall. As initial condition, a fully developed temperature field, based on the solution of a steady-state equation without the coupling terms to the PSD, was chosen.

Last, the behaviour of the PSD has to be modelled. Currently, only a model is available which is based on the idealisation that the particles are of spherical shape, such that they can be prescribed completely by their diameter. In practice, the particles are rather needle-shaped. With this idealisation, the equation for the PSD is given by

$$\frac{\partial f}{\partial t} + G(c,T)\frac{\partial f}{\partial L} + \mathbf{u}\cdot\nabla f = A_+ + A_-, \tag{11}$$

where A_+ is the source of the aggregation model and A_- is its sink. For modelling the aggregation, the volume of the urea particles is considered. It is assumed that the volume is proportional to the cube of the diameter $V = k_V L^3$, with $k_V > 0$. This means, all particles are assumed to be of the same shape, e.g., balls or cubes. Then, the PSD with respect to the volume is given by

$$f_V(V) = f_V(k_V L^3) = \frac{f(L)}{k_V}\frac{1}{3L^2} \quad \left[\frac{1}{\mathrm{m}^6}\right]. \tag{12}$$

The source term describes the amount of particles of volume V which are created by the aggregation of two particles with volume V' and $V - V'$, $V' \in (0, V)$. This is given by

$$A_{+,V} = \frac{1}{2}\int_0^V \kappa_{\text{agg}}(V-V', V') f_V(V-V') f_V(V')\, dV'. \tag{13}$$

The factor $1/2$ arises since there are two realisations of this event: the first particle has volume V', the second has volume $V - V'$, and vice versa. The sink term describes the amount of particles of volume V that vanish because they are consumed by aggregations with other particles of volume $V' \in (0, V_{\max})$

$$A_{-,V} = -\int_0^{V_{\max}} \kappa_{\text{agg}}(V,V') f_V(V) f_V(V')\, dV' = -f_V(V)\int_0^{V_{\max}} \kappa_{\text{agg}}(V,V') f_V(V')\, dV'. \tag{14}$$

The sum of $A_{+,V}$ and $A_{-,V}$ gives the change of particles of volume V due to the aggregation. The change with respect to the diameter is then obtained by

$$A_+ + A_- = 3k_V(A_{+,V} + A_{-,V})\, L^2,$$

Prepared using fldauth.cls DOI: 10.1002/fld

compare (12). The aggregation kernel is the product of two factors

$$\kappa_{\text{agg}}(V,V') = p_{\text{col}}(V,V')p_{\text{eff}}(V,V') \quad \left[\frac{\text{m}^3}{\text{s}}\right].$$

The first factor gives the probability of the collision of particles with volume V and V'. The efficiency of the collisions, i.e. the amount of collisions which actually lead to aggregations, is described by the second factor. Due to the lack of models, this factor is chosen to be constant. This constant can be included into scaling factors for the individual terms of the following kernel, see [17, 18],

$$\begin{aligned}\kappa_{\text{agg}}(V,V') &= C_{\text{br}}\frac{2k_BT}{3\mu}\left(\sqrt[3]{V}+\sqrt[3]{V'}\right)\left(\frac{1}{\sqrt[3]{V}}+\frac{1}{\sqrt[3]{V'}}\right) \\ &\quad + \frac{C_{\text{sh}}}{k_V}\sqrt{2\nabla\mathbf{u}:\nabla\mathbf{u}}\left(\sqrt[3]{V}+\sqrt[3]{V'}\right)^3 \left[\frac{\text{m}^3}{\text{s}}\right],\end{aligned} \tag{15}$$

where $k_B = 1,3806504\ 10^{-23}$ [J/K] is the Boltzmann constant and $C_{\text{br}}, C_{\text{sh}}$ are constants that have to be calibrated on the basis of the experimental data. The first term in (15) is Brownian-motion-generated. It is important for small particles since in this case the last factor becomes large. The second term is shear-induced [19] and it becomes important if both particles are large.

The initial condition is given by

$$f(0,\mathbf{x},L) = 0 \quad \text{in } \Omega\times(L_{\min},L_{\max}),$$

i.e. there are no particles in the flow domain. Boundary conditions are necessary at the closure of the inflow boundaries

$$f(t,\mathbf{x},L) = \begin{cases} f_{\text{in}}(t,\mathbf{x},L), & \mathbf{x}\in\Gamma_{\text{in}} \\ \dfrac{B_{\text{nuc}}}{G(c,T)}, & \text{at } L = L_{\min}, \text{ if } G(c,T) > 0. \end{cases}$$

The PSD at Γ_{in} is given by experimental data, see Section 4.

Numerical simulations are based on dimensionless equations. For their derivation, the following reference quantities were used: a reference velocity u_∞ [m/s], a reference length scale l_∞ [m], a reference concentration c_∞ [mol/m^3], a reference temperature T_∞ [K], a reference value for the PSD f_∞ [1/m^4] and a reference diameter of the particles L_∞ [m]. The reference

DOI: 10.1002/fld

pressure was defined by $p_\infty = \rho u_\infty^2$ [Pa] and the reference time by $t_\infty = l_\infty / u_\infty$ [s]. The derivation of the dimensionless equations with these reference values proceeds in a standard way.

3. THE NUMERICAL METHODS

A schematic sketch of the couplings in the considered population balance system is presented in Fig. 1. All spatial discretisation were performed on a hexahedral grid. The flow field, the initial temperature distribution and the initial concentration were computed in a preprocessing step.

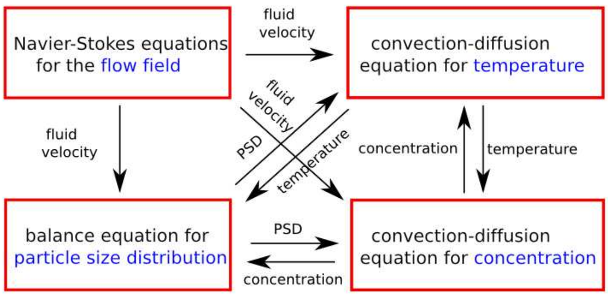

Figure 1. Couplings of the equations in the population balance system for the urea synthesis.

The computation of the flow field requires only a discretisation in space. For this purpose, the inf-sup stable Q_2/P_1^{disc} finite element was used. This finite element is a popular choice [20] as it combines a high accuracy and the possibility of solving the arising saddle point problems efficiently [21, 22].

The equations for concentration, temperature and PSD form a coupled system. This was solved iteratively, where a step of the iteration started with solving the equation for the temperature, followed by solving the equation for the concentration and finished with the equation for the PSD. Different discretisations were used for the equations defined on the three-dimensional domain Ω (concentration, temperature) and the equation for the PSD, which is given on a four-dimensional domain.

DOI: 10.1002/fld

The temperature and the concentration are governed by convection-dominated equations. These equations were discretised in time with the Crank–Nicolson scheme. In space, a stabilised finite element method, based on the Q_1 finite element, was applied. As stabilisation, the linear FEM-FCT scheme was used [12]. This scheme has been proven to be among the best performing stabilised finite element methods for time-dependent convection-dominated scalar equations in [23, 24]. In particular, it does not lead to under- and overshoots of the computed solutions.

Equation (11) for the PSD is a linear convection-dominated integro partial differential equation that is defined for each discrete time in a four-dimensional domain. In [10], several schemes were explored for solving this kind of equation. It was found that for laminar flow fields, simple and inexpensive schemes give similar results for quantities of interest compared with more accurate and expensive schemes. In particular, finite element schemes are rather expensive because of the costs for assembling the matrices (the number of quadrature points scales exponentially with the dimension). Based on our experience, a forward Euler upwind finite difference method (FWE-FDM) was applied for the discretisation of (11).

In the discretisation of the individual equations of the coupled system, always the latest values of the other unknowns were used to evaluate the coupling terms. The iteration for solving the coupled system was stopped if the sum of the Euclidian norms of the residual vectors for concentration and temperature was below a prescribed tolerance.

Much more small particles were contained in the fluid than large particles. Therefore, it is natural to use a grid for the PSD, with respect to the volume of the particles, that is refined towards the smallest particles. For the algorithm, which is used for evaluating the aggregation integrals, it is essential that this local refinement is not arbitrary but that the locally refined grid can be decomposed into uniform grids at each level as it is illustrated in Fig. 2. The ansatz space $\mathcal{S}$ for the PSD was chosen to consist of piecewise linear functions.

Prepared using **fldauth.cls**
DOI: 10.1002/fld

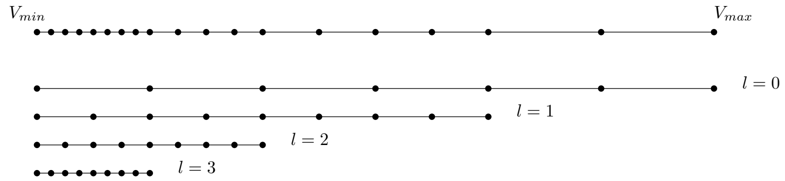

Figure 2. Decomposition of the locally refined grid for the PSD.

Note that both terms in the considered aggregation kernel have separable structure, i.e. the aggregation kernel can be written in the form

$$\kappa_{\text{agg}}(V, V') = \sum_{i=1}^{k} a_i(V) b_i(V').$$

Then, the integral term $A(V)$ becomes

$$\begin{aligned} A(V) &= A_+(V) + A_-(V) = \\ &= \frac{1}{2}\int_0^V \kappa_{\text{agg}}(V - V', V') f_V(V - V') f_V(V')\, dV' - f_V(V) \int_0^\infty \kappa_{\text{agg}}(V, V') f_V(V')\, dV' \\ &= \sum_{i=1}^{k} \left[\frac{1}{2}\int_0^V a_i(V - V') b_i(V') f_V(V - V') f_V(V') dV' \right. \\ &\quad \left. - f_V(V) a_i(V) \int_0^\infty b_i(V') f_V(V')\, dV' \right]. \end{aligned}$$

The evaluation of the sink term is not difficult since only one-dimensional integrals have to be computed. The source term in this formulation is the sum of convolutions $\varphi_i * \psi_i$, where $\varphi_i = a_i f$ and $\psi_i = b_i f$. The functions $a_i(V)$ and $b_i(V)$ were approximated by piecewise constants on the same grid as $f_V(V)$. Legendre polynomials were used as an orthonormal basis of $\mathcal{S}$. Thanks to some known facts about Legendre polynomials, the convolution can be computed with the complexity $\mathcal{O}(n \log n)$, where n is the number of grid points. In essence, it turns out that some discrete convolutions have to be computed, which can be easily performed using the fast Fourier transform ($\mathcal{FFT}$). For details of the rather involved algorithm, the reader is referred to [13, 14, 15].

The exact convolution $\omega_{\text{exact}} = \sum_{i=1}^{k} \varphi_i * \psi_i$ does not belong to the ansatz space $\mathcal{S}$. In the simulations, the L^2 projection ω_{comp} of ω_{exact} into the ansatz space was used. An issue in using

DOI: 10.1002/fld

an approximation of ω_{exact} might be mass conservation. However, since $\omega_{\text{exact}} - \omega_{\text{comp}}$ is L^2 orthogonal to all piecewise linear functions, one obtains for all intervals $[V_i, V_{i+1}]$

$$\text{mass}_i(\omega_{\text{exact}}) = \int_{V_i}^{V_{i+1}} V'\omega_{\text{exact}}(V')\, dV' = \int_{V_i}^{V_{i+1}} V'\omega_{\text{comp}}(V')\, dV' = \text{mass}_i(\omega_{\text{comp}}),$$

i.e. the mass (volume) is locally preserved. The only change in total mass that might occur comes from the fact that the support of the convolution is larger than the support of the convolved functions. In the case of aggregation, only non-negative contributions will be neglected by not considering the complete support of the convolution such that the mass will always decrease. This might be crucial for long time simulations. To avoid the decrease of mass, a correction to the aggregation term is computed as follows

$$A(V) := A(V) - \text{mass}(A(V))\frac{2}{V_{\max}^2 - V_{\min}^2},$$

where $V_{\min}$ and $V_{\max}$ are the smallest and largest volume of the particles, respectively. Then, although the local mass conservation is violated, the total mass of the computed aggregation term is zero, which is in accordance with the modelling of this term.

A different correction would be the L^2 projection of $A(V)$ into the space of mass-conserved functions $\{B(V) \ : \ \int_{V_{\min}}^{V_{\max}} V'B(V')\, dV' = 0\}$, which has the form

$$A(V) := A(V) - \text{mass}(A(V))\frac{3V}{V_{\max}^3 - V_{\min}^3}.$$

Due to the factor V in the correction part, mainly the values $A(V)$ for large volumes will be affected. For the aggregation term, these values will increase to compensate the loss of mass due to cutting the support of the convolution. We could observe that this might result in unnaturally large values for the aggregation term and then for the PSD, in the last interval for the internal coordinate. The same happened with the strategy proposed in [14], which applies a correction only in the last interval. Hence, we do not recommend these approaches.

Prepared using **fldauth.cls** DOI: 10.1002/fld

4. THE EXPERIMENTAL DATA AND THEIR INCORPORATION INTO THE SIMULATIONS

The experiments which will be considered are described in [11]. Data for space-time-averaged normalised volume fractions are provided, which were obtained by measurements using a microscope with a flow-through cell.

In the experiments, the flow rate at the inlet V_r [ml/min] $= V_r/60$ [cm^3/s] was prescribed. This data has to be matched by the flow rate of the used boundary condition at the inlet (2)

$$U_{\rm in} \int_{\Gamma_{\rm in}} (\Psi(\xi,\eta),0,0)^T \ d\xi d\eta \ \left[\frac{\rm cm^3}{\rm s}\right].$$

It follows

$$U_{\rm in} = \frac{V_r}{60\int_{\Gamma_{\rm in}} (\Psi(\xi,\eta),0,0)^T \ d\xi d\eta},$$

where the integral in the nominator can be approximated by numerical quadrature.

The boundary conditions for the temperature are provided from the experiments as given in (10). Also the inlet condition of the concentration is controlled as given in (6).

Concerning the inlet condition of the PSD, particles were injected into the channel only in the time interval $[0, t_{\rm inj}]$ s with $t_{\rm inj} = 5$ s. From the experiments, a space-time-averaged inlet condition is provided, such that a boundary condition of the form

$$f_{\rm in}(t,\mathbf{x},L) = \begin{cases} f_{\rm inj}(L) & \text{for } t\in[0,t_{\rm inj}]\ s,\ \mathbf{x}\in\Gamma_{\rm in}, \\ 0 & \text{else,} \end{cases}$$

can be applied. The particles were contained in a solution with volume $V_{\rm inj}$ [m^3], which was injected into the domain in $[0, t_{\rm inj}]$, i.e.

$$V_{\rm inj} = \int_0^{t_{\rm inj}} V_r \ dt = \frac{t_{\rm inj} V_r}{60\cdot 10^6} \ [{\rm m}^3].$$

It follows that the total number of particles which were injected is given by

$$\int_{V_{\rm inj}} \int_{L_{\min}}^{L_{\max}} f_{\rm inj}(L) \ dL \ d\mathbf{x} = V_{\rm inj} \int_{L_{\min}}^{L_{\max}} f_{\rm inj}(L) \ dL = \int_{L_{\min}}^{L_{\max}} \frac{t_{\rm inj} V_r}{6\cdot 10^7} f_{\rm inj}(L) \ dL. \qquad (16)$$

The experiments provide the distribution of the number of particles per diameter $f_{L,\rm seed}(L)$ [1/m] in $V_{\rm inj}$. This number was identical in all experiments, see Fig. 3 for a

Prepared using fldauth.cls
DOI: 10.1002/fld

presentation of this curve. Integration of $f_{L,\mathrm{seed}}(L)$ gives the total number of particles, i.e., to obtain the same total number of particles as given in (16)

$$f_{L,\mathrm{seed}}(L) = \frac{t_{\mathrm{inj}} V_r}{6 \cdot 10^7} f_{\mathrm{inj}}(L) \quad \Longrightarrow \quad f_{\mathrm{inj}}(L) = \frac{6 \cdot 10^7}{t_{\mathrm{inj}} V_r} f_{L,\mathrm{seed}}(L) \quad L \in [L_{\min}, L_{\mathrm{mas}}],$$

should hold. This expression gives the required value for the boundary condition of the PSD at the inlet of the domain.

The experiments provide space-time-averaged evaluations of the volume fraction of the PSD. Let $\mathbf{x} \in \Omega$, then the volume fraction is defined by

$$q_3(t, \mathbf{x}, L) = \frac{L^3 f(t, \mathbf{x}, L)}{\int_{L_{\min}}^{L_{\max}} L^3 f(t, \mathbf{x}, L)\, dL}.$$

The normalised volume fraction of the inlet condition for the PSD is given in Fig. 3. Similarly derived profiles are provided at the outlet of the experimental domain ($x = 200$ cm) for different flow rates. These profiles will be used in the comparison with the numerical results.

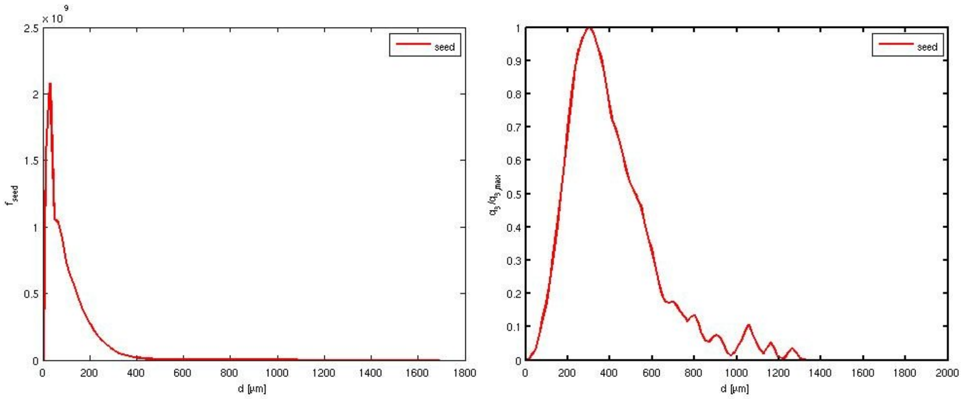

Figure 3. $f_{L,\mathrm{seed}}(L)$ at the inlet (left) and the normalised volume fraction of the PSD at the inlet (right).

5. NUMERICAL STUDIES

5.1. *The general setup*

Experimental data were available for two setups differing in the flow rate at the inlet. Both setups will be considered in the numerical studies. An important goal was the calibration of

Prepared using fldauth.cls DOI: 10.1002/fld

the unknown model parameters in the aggregation kernel (15) in such a way that a good agreement to the experimental data was obtained. This data consists of a space-time-averaged normalised volume fraction at the outlet. A second important aspect of the numerical studies was the investigation of the PSD at different points at the outlet. It will be shown that, e.g., the PSD in the centre of the channel possesses a considerably different form compared with the PSDs in points which are closer to the walls.

In the numerical simulations, the following reference values were used

$$\begin{aligned} &l_\infty = 0.01 \text{ m},\ u_\infty = 0.01 \,\frac{\text{m}}{\text{s}},\ T_\infty = 1 \text{ K},\ c_\infty = 1000 \,\frac{\text{mol}}{\text{m}^3}, \\ &L_\infty = 5\cdot 10^{-3} \text{ m},\ f_\infty = 10^{13}\,\frac{1}{\text{m}^4},\ \tilde{L}_{\min} = 2.5\ 10^{-6} \text{ m},\ \tilde{L}_{\max} = 5\cdot 10^{-3} \text{ m}. \end{aligned}$$

The flow domain is very long compared with its thickness and there is a preferred direction of the flow. This enables the use of an a priori adapted grid with anisotropic grid cells, see Fig. 4. In this figure, the y- and z–coordinates are scaled for a better presentation. The aspect ratio (ratio of largest edge and smallest edge) of the mesh cells is small at the inlet to resolve the recirculation zone. It becomes larger towards the outlet. At the end of the flow domain, the mesh cells have an aspect ratio of 30.

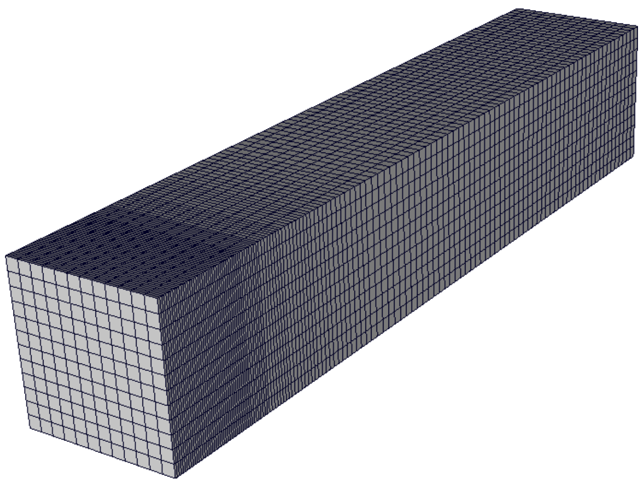

Figure 4. The computational grid, flow domain not to scale (scaled up by factor 40 in y- and z-direction).

Prepared using **fldauth.cls** DOI: 10.1002/fld

The Q_2/Q_1^{disc} discretisation of the stationary Navier–Stokes equations (1) – (4) led to 496 875 velocity degrees of freedom (d.o.f.) and to 76 032 pressure d.o.f. on the grid presented in Fig. 4. As mentioned already above, for both flow rates from the experiments, the Navier–Stokes equations have to be solved only once in a preprocessing step.

The number of d.o.f. for the concentration of dissolved urea and for the temperature on the grid from Fig. 4 was 22 477.

Especially small particles were injected into the fluid, see Fig. 3. For this reason, the grid for the internal coordinate is locally refined for small diameters. As explained in Section 3, the computation of the aggregation integrals is based on a grid with respect to the mass of the particles which has to possess certain properties. This issue was taken into account in the construction of the grid with respect to the diameter, see Fig. 5 for both grids. The grid with respect to the mass is piecewise equidistant. It possesses 94 nodes which leads to 2 112 838 d.o.f. for the PSD.

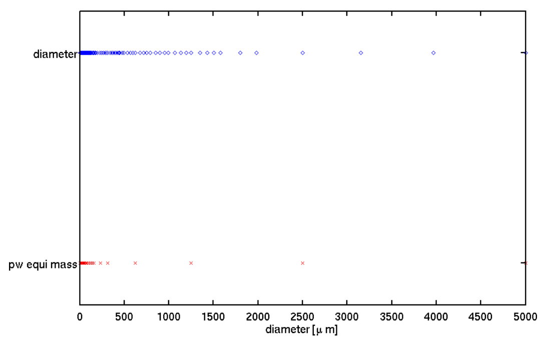

Figure 5. The grid with respect to the internal coordinate, diameter (top) and mass (bottom).

As noted in Section 2, the initial temperature and the initial concentration were computed in a preprocessing step. The time step was set to be $\Delta t = 0.1$ s. Because of the somewhat explosive start at the beginning of the simulations, a smaller length of the time step was applied in $[0, 10]$ s. All simulations were performed with the code MooNMD [25].

It was checked that with smaller time steps the results practically do not change. For the sake of brevity, these studies are not included here.

Prepared using fldauth.cls
DOI: 10.1002/fld

5.2. Experiment with flow rate $\tilde{V}_r = 30$ ml/min

First, an experiment was studied that was conducted with a flow rate of $\tilde{V}_r = 30$ ml/min. The Reynolds number based on the integral mean velocity at the inlet $U = 4.5$ cm/s, the diameter of the channel $L = 1$ cm and the kinematic viscosity of ethanol $\nu = \mu/\rho = 1.3612\ 10^{-6}$ m^2/s is given by $Re \approx 331$. The stationary flow field at the inlet of the channel is shown in Fig. 6.

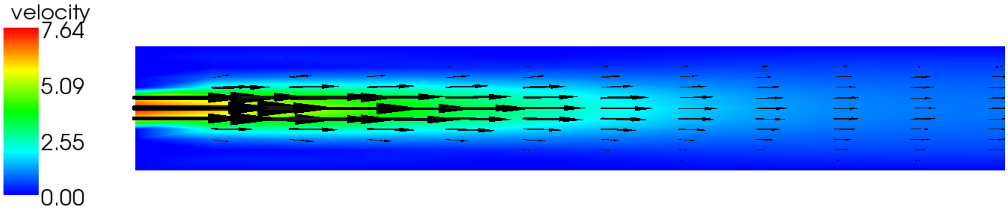

Figure 6. Experiment with flow rate $\tilde{V}_r = 30$ ml/min; cut of the stationary velocity field at the inlet of the channel.

Based on the residence time of the particles, the data at the outlet of the experimental domain at $x = 200$ cm were studied in the interval $[200, 300]$ s. For each grid point at the outlet, the PSD was added and then a time-average was computed. After this, a spatial averaging was calculated and from this the normalised volume fraction for these space-time-averaged values was derived. This normalised volume fraction was utilised for the calibration of the unknown parameters $C_{\rm br}$ and $C_{\rm sh}$ in the aggregation kernel (15). Results for different values of the parameters are presented in Fig. 7. Comparing the experimental data at the outlet with those at the inlet, Fig. 3, one can observe that the curve of the normalised volume fraction moves to the right. The increase of the number of larger particles due to aggregation and growth is clearly visible. A rather good agreement of the experimental and the numerical data could be obtained with $C_{\rm br} \simeq 2 \cdot 10^5$ and $C_{\rm sh} \simeq 0.01$.

For these parameters, the PSD at the outlet was studied in more detail. Fig. 8 presents the time-averaged PSD which left the domain at different nodes in the outlet plane and Fig. 9 shows the corresponding normalised volume fractions. Nodes on a line between the wall and the centre of the channel which is parallel to the plane $z = 0$ and nodes on a line between a

DOI: 10.1002/fld

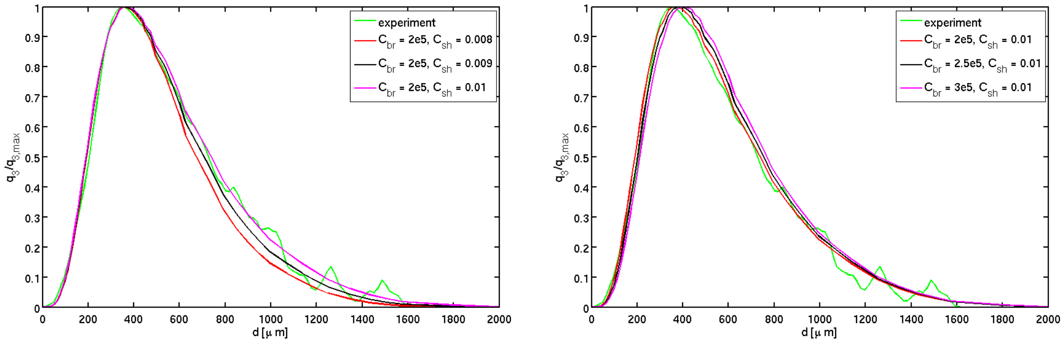

Figure 7. Flow rate $\tilde{V}_r = 30$ ml/min; space-time-averaged normalised volume fraction at the outlet for different parameters C_{br} and C_{sh}.

corner of the outlet and the centre of the channel were considered. First, it can be seen that the most particles could be found in the centre of the channel, i.e. the bulk of the particles followed the flow very well. The closer the node is to the wall, the less particles were observed. In particular, the number of particles in the nodes with a distance less or equal than $1/6$ cm to one of the walls was negligible (green and cyan curves).

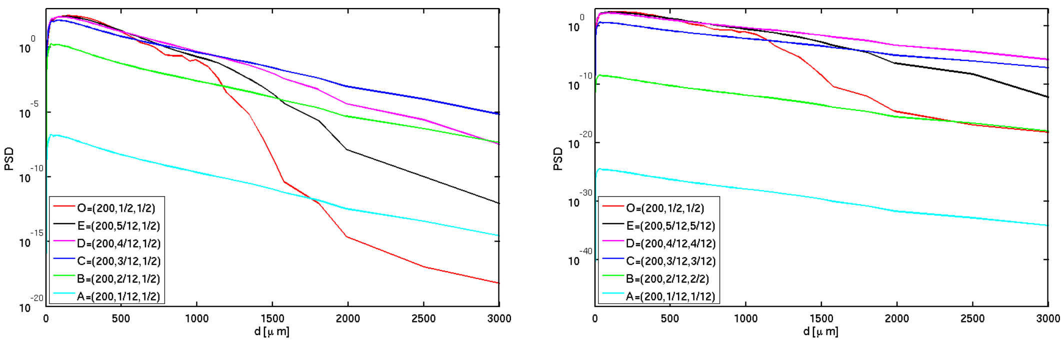

Figure 8. Flow rate $\tilde{V}_r = 30$ ml/min; time-averaged PSD at the outlet for different nodes, $C_{\mathrm{br}} = 2 \cdot 10^5$ and $C_{\mathrm{sh}} = 0.01$.

The distribution of the particles with respect to the diameter was very different for different nodes. In the centre of the channel, most of the small particles were observed but only very few large particles. The majority of the large particles could be found in regions that are $1/4 - 1/3$ cm away from the centre of the channel. This different behaviour can be seen also well in the normalised volume fractions in Fig. 9. The results for the individual nodes illustrate

Prepared using fldauth.cls
DOI: 10.1002/fld

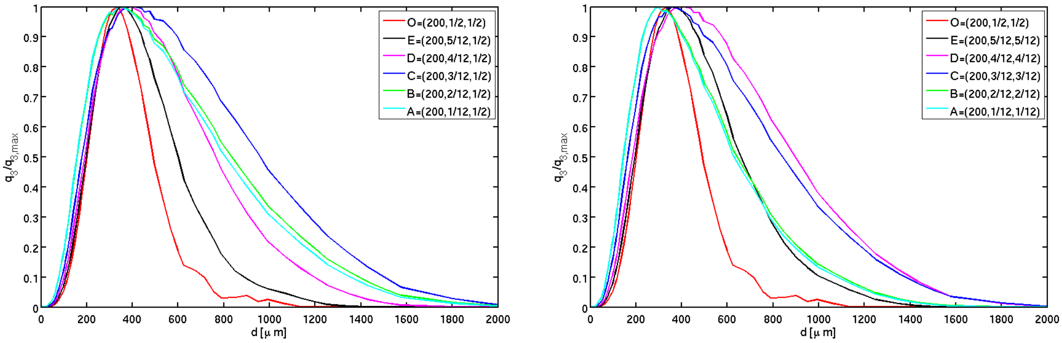

Figure 9. Flow rate $\tilde{V}_r = 30$ ml/min; time-averaged normalised volume fraction at the outlet for different nodes, $C_{\rm br} = 2 \cdot 10^5$ and $C_{\rm sh} = 0.01$.

in a good way the effect of the different parts of the aggregation kernel (15). In the centre of the channel, the shear of the flow field was comparatively small. For this reason, the second term in (15), which is of importance for the aggregation of large particles, did not possess much impact. Away from the centre, the shear was larger. Hence, the second term of (15) became dominant in the kernel and larger particles were generated by the aggregation.

5.3. Experiment with flow rate $\tilde{V}_r = 90$ ml/min

A second experiment was conducted with the flow rate $\tilde{V}_r = 90$ ml/min. Also this flow rate led to a stationary flow field, see Fig. 10, with $Re \approx 992$ based on the same reference values as for the first example.

Since the flow is considerably faster for $\tilde{V}_r = 90$ ml/min than in the first experiment, the residence time of the particles is shorter. In particular, there will be less time to build large particles by aggregation and growth compared with the first experiment.

Numerical results for space-time-averaged normalised volume fractions at the outlet are presented in Fig. 11. Time-averaging of the PSD was performed in $[60 - 110]$ s. Again, it was possible to calibrate the parameters in the aggregation kernel in such a way that a good agreement with the experimental data could be obtained. Appropriate parameters are $C_{\rm br} \simeq 3 \cdot 10^5$ and $C_{\rm sh} \simeq 0.004$. These parameters differ somewhat from the parameters obtained for the first example, but they are of the same order of magnitude.

Prepared using fldauth.cls
DOI: 10.1002/fld

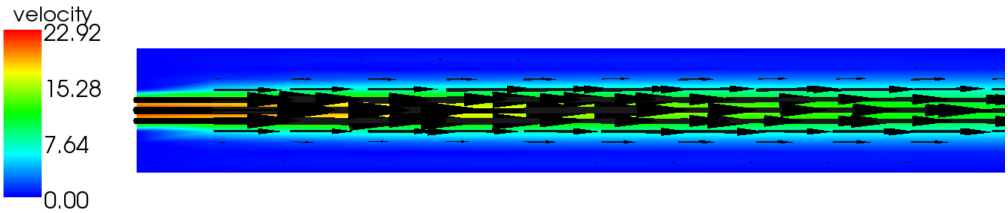

Figure 10. Experiment with flow rate $\tilde{V}_r = 90$ ml/min; cut of the stationary velocity field at the inlet of the channel.

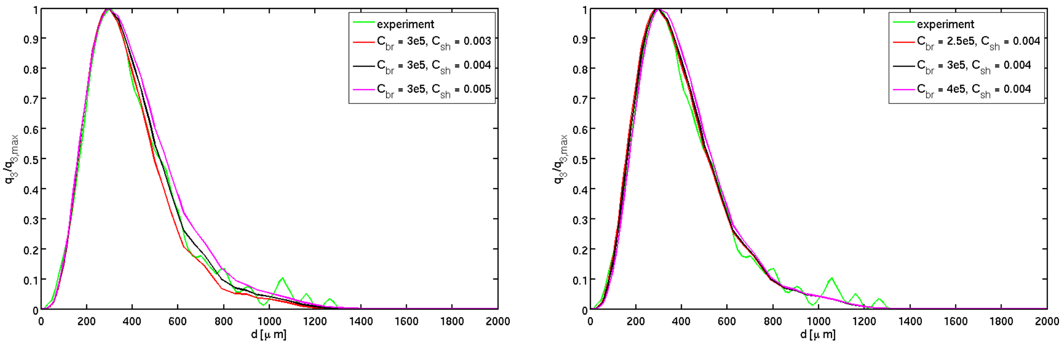

Figure 11. Flow rate $\tilde{V}_r = 90$ ml/min; space-time-averaged normalised volume fraction at the outlet for different parameters $C_{\rm br}$ and $C_{\rm sh}$.

More detailed studies of the PSD at the outlet are presented in Figs. 12 and 13. The principal behaviour is the same as for the first example. Most of the small particles but almost no large particles can be observed in the centre of the channel. The large particles arrive away from the centre. In the points which are too close to the walls, the amount of particles is negligible. In contrast to the first example, the amount of very large particles is much smaller, compare the scalings. This is due to the shorter residence time.

5.4. Discussion of the results and further aspects of the simulations

For both experimental setups, it was possible to identify model parameters $C_{\rm br}$ and $C_{\rm sh}$ such that a very good agreement with the experimental data (space-time-averaged normalised volume fraction at the outlet) could be obtained. The optimal values for $C_{\rm br}$ and $C_{\rm sh}$ differ somewhat but they are of the same order of magnitude. We think that these differences are

Prepared using fldauth.cls DOI: 10.1002/fld

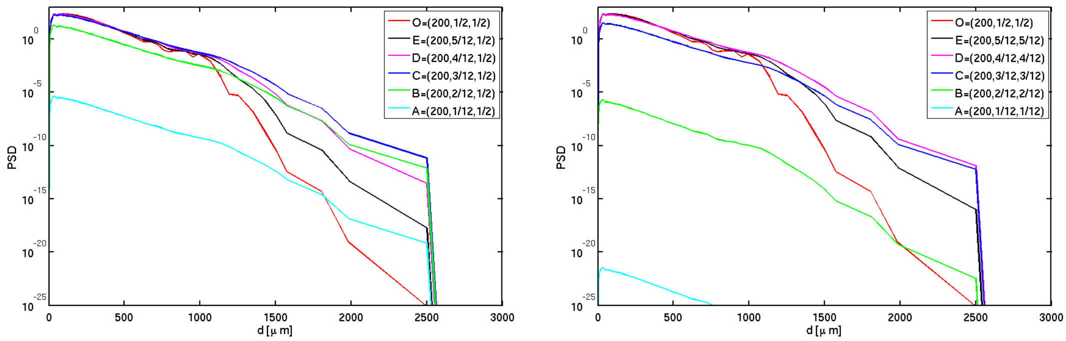

Figure 12. Flow rate $\tilde{V}_r = 90$ ml/min; time-averaged PSD at the outlet for different nodes, $C_{\text{br}} = 3 \cdot 10^5$ and $C_{\text{sh}} = 0.004$.

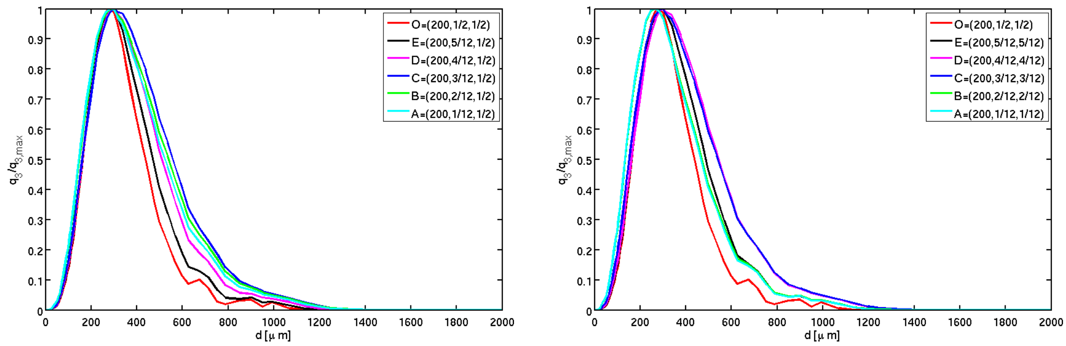

Figure 13. Flow rate $\tilde{V}_r = 90$ ml/min; time-averaged normalised volume fraction at the outlet for different nodes, $C_{\text{br}} = 3 \cdot 10^5$ and $C_{\text{sh}} = 0.004$.

caused by the following reasons. First, as already discussed in Section 2, the idealisation of spherical particles was used in modelling the equation for the PSD. Second, the observed sizes of the diameters in the measurements were not diameters of three-dimensional particles but diameters of projections of real particles into a plane. Both issues led of course to some errors in the measurements. The calibration of C_{br} and C_{sh} could compensate these errors quite well for each experiment. But this compensation led to somewhat different values for C_{br} and C_{sh}. And last, (15) is only a model with an unknown modelling error.

The impact of both parts of the aggregation kernel (15) could be observed well in detailed studies of the PSD in the nodes at the outlet. The numerical results correspond completely to the expectations.

DOI: 10.1002/fld

The simulations were performed on HP BL2x220c computers with 2933 MHz Xeon processors. Simulating one time step took around 45 – 60 seconds, including the calculation of all data for evaluating the numerical simulations. The most expensive part was the computation of the aggregation which needed around 75 % of this time.

6. SUMMARY AND OUTLOOK

This paper presented a numerical method for solving a population balance system consisting of equations defined in a three-dimensional domain (Navier–Stokes equations, convection-diffusion equations for mass and energy balances) and an equation defined in a four-dimensional domain (PSD). The considered process of urea synthesis is aggregation-dominated. To our best knowledge, the presented method is among the few approaches for solving a coupled population balance system with aggregation which is defined in domains with three and four dimensions.

Two experimental setups were considered. For both, it was possible with the proposed method to calibrate unknown model parameters in the aggregation kernel in such a way that good agreements to available experimental data were achieved. The obtained values of the parameters for both experiments are of the same order of magnitude. Several possible reasons for the observed differences were pointed out: the idealised assumption of spherical particles in the modelling, the observations of projections of particles in the experiments and the modelling error of the kernel itself.

The crucial next step will be the extension of the model to needle-shaped particles as they are occur in practice. This is a challenge for modelling, measurements and numerical simulations as well. To describe needle-shaped particles, two internal coordinates are necessary, e.g., the length and the diameter of the cross-section of the particles. The equation for the corresponding PSD will be defined in a five-dimensional domain.

Considering the same flow domain as in the present paper, the five-dimensional domain will be a tensor product of intervals. Then, the extension of the forward Euler upwind finite difference method for discretising the convective part of the PSD equation is straightforward.

Prepared using **fldauth.cls** DOI: 10.1002/fld

However, in future it is intended to use more accurate schemes for this part, like ENO finite difference methods, see [26] for promising studies of such methods. Another important task will be the extension of the algorithm for computing the aggregation integrals. The simulation of coupled population balance systems with two internal coordinates, including aggregation, without applying any model simplification to obtain moment-based methods, would provide new contributions to the understanding of population balanced processes.

ACKNOWLEDGEMENTS

The research of A. Khachatryan was supported by the Bundesministerium für Bildung und Forschung (BMBF), grant 03HAPAA4. The research of C. Suciu was supported by the Bundesministerium für Bildung und Forschung (BMBF), grant 03JOPAA5.

REFERENCES

1. Gradl J, Schwarzer HC, Schwertfirm F, Manhart M, Schmid HJ, Peukert W. Precipitation of nanoparticles in a T–mixer: Coupling the particle population dynamics with hydrodynamics through direct numerical simulation. *Chem. Engrg. Proc.* 2007; :908 – 916.
2. Kulikov V, Briesen H, Grosch R, von Wedel L, Yang A, Marquardt W. Modular dynamic simulation for integrated particulate processes by means of tool integration. *Chem. Engrg. Sci.* 2005; **60**:2069 – 2083.
3. Kulikov V, Briesen H, Marquardt W. A framework for the simulation of mass crystallization considering the effect of fluid dynamics. *Chem. Engrg. Proc.* 2007; **60**:886 – 899.
4. Schwarzer HC, Schwertfirm F, Manhart M, Schmid HJ, Peukert W. Predictive simulation of nanoparticle precipitation based on the population balance equation. *Chem. Engrg. Sci.* 2006; :167 – 181.
5. McGraw R. Description of aerosol dynamics by the quadrature method of moments. *Aerosol Science and Technologie* 1997; :255 – 265.
6. Marchisio D, Fox R. Solution of population balance equations using the direct quadrature method of moments. *Journal of Aerosol Science* 2005; **36**(1):43–73.
7. John V, Angelov I, Öncül AA, Thévenin D. Techniques for the reconstruction of a distribution from a finite number of its moments. *Chem. Engrg. Sci.* 2007; **62**:2890 – 2904.
8. de Souza L, Janiga G, John V, Thévenin D. Reconstruction of a distribution from a finite number of moments with an adaptive spline-based algorithm. *Chem. Engrg. Sci.* 2010; **65**:2741 – 2750.
9. John V, Mitkova T, Roland M, Sundmacher K, Tobiska L, Voigt A. Simulations of population balance systems with one internal coordinate using finite element methods. *Chem. Engrg. Sci.* 2009; **64**:733 – 741.

10. John V, Roland M. On the impact of the scheme for solving the higher–dimensional equation in coupled population balance systems. *Int. J. Numer. Meth. Engrg.* 2010; **82**:1450 – 1474.

11. Borchert C, Sundmacher K. Crystal aggregation in a flow tube: image-based observation. *Chem. Eng. Technol.* 2011; :545 – 556.

12. Kuzmin D. Explicit and implicit FEM–FCT algorithms with flux linearization. *J. Comput. Phys.* 2009; **228**:2517 – 2534.

13. Hackbusch W. On the efficient evaluation of coalescence integrals in population balance models. *Computing* 2006; **78**:145 – 159.

14. Hackbusch W. Approximation of coalescence integrals in population balance models with local mass conservation. *Numer. Math.* 2007; **106**:627 – 657.

15. Hackbusch W. Convolution of hp-functions on locally refined grids. *IMA Journal of Numerical Analysis* 2009; **29**:960 – 985.

16. Turek S. *Efficient Solvers for Incompressible Flow Problems: An Algorithmic and Computational Approach*, *Lecture Notes in Computational Science and Engineering*, vol. 6. Springer, 1999.

17. Berglund K. Analysis and measurment of crystillization utilizing the population balance. *Handbook of Industrial Crystallization*, Myerson A (ed.). second edn., Butterworth-Heinemann, 2002.

18. Lindenberg C, Schöll J, Vicum M, Brozio J. L-glutamic acid precipitation: Agglomeration effects. *Crystal Growth & Design* 2008; **8**:224 – 234.

19. Smoluchowski M. Versuch einer mathematischen Theorie der Koagulationskinetik kolloider Lösungen. *Z. Phys. Chem.* 1917; **92**:129 – 168.

20. Gresho P, Sani R. *Incompressible Flow and the Finite Element Method*. Wiley, Chichester, 2000.

21. John V, Matthies G. Higher order finite element discretizations in a benchmark problem for incompressible flows. *Int. J. Num. Meth. Fluids* 2001; **37**:885 – 903.

22. John V. Higher order finite element methods and multigrid solvers in a benchmark problem for the 3D Navier–Stokes equations. *Int. J. Num. Meth. Fluids* 2002; **40**:775 – 798.

23. John V, Schmeyer E. Stabilized finite element methods for time–dependent convection–diffusion–reaction equations. *Comput. Methods Appl. Mech. Engrg.* 2008; **198**:475 – 494.

24. John V, Schmeyer E. On finite element methods for 3d time–dependent convection–diffusion–reaction equations with small diffusion. *BAIL 2008 – Boundary and Interior Layers*, *Lecture Notes in Computational Science and Engineering*, vol. 69, Springer, 2009; 173 – 182.

25. John V, Matthies G. MooNMD - a program package based on mapped finite element methods. *Comput. Visual. Sci.* 2004; **6**:163 – 170.

26. John V, Novo J. On (essentially) non-oscillatory discretizations of evolutionary convection-diffusion equations. *Preprint*, WIAS Berlin 2011.

DOI: 10.1002/fld